Inorg. Chem. **2002**, *41*, 205–218

Coupled Redox Potentials in Manganese and Iron Superoxide Dismutases from Reaction Kinetics and Density Functional/ Electrostatics Calculations

Wen-Ge Han,* Timothy Lovell, and Louis Noodleman*

Department of Molecular Biology, TPC15, The Scripps Research Institute, 10550 N. Torrey Pines Road, La Jolla, California 92037

Received April 2, 2001

A methodology for determining the coupled redox potentials ($\Delta E_{redox}°$(coupled)) of manganese and iron superoxide dismutases (Mn(Fe)SODs), from the standard redox potential of reaction ($O_2^- + 2H^+ + e^- \rightarrow H_2O_2$) and the experimental kinetic rate constants of Mn(Fe)SOD proteins, has been presented for the first time. A combined density functional (DF) and electrostatic protein/reaction field (DF/electrostatics) model has also been applied to seven protein structures, to study the structural, energetic, simple redox potential, pK_a, and coupled redox potential properties associated with each active site. The quantum cluster active site models, which include the metal, first shell ligands, represented by amino acid side chains and a solvent derived ligand, and the second shell H-bonding partners, were taken from the crystal structures, and geometry was optimized in four kinds of states: oxidized (III) and reduced (II) states with either a H_2O molecule or a OH^- group as the fifth coordinated ligand. We conclude from the calculations that the oxidized and reduced Mn(Fe)SODs are in the $Mn^{3+}(Fe^{3+})(OH^-)$ and $Mn^{2+}(Fe^{2+})(H_2O)$ forms, respectively; proton transfers will happen in both steps of the dismutation of superoxide anion (O_2^-), and the proton-transfer reactions will occur prior to or concerted with the electron transfer from O_2^- group to the $Mn^{3+}(Fe^{3+})$SOD metal center. The $\Delta E_{redox}°$(coupled) of *E. coli* FeSOD calculated by the DF/electrostatics method is 0.16 V, which is very close to the experimental value of 0.25 V. The absolute values of $\Delta E_{redox}°$(coupled) for *T. thermophilus,* human wild-type, and mutant Q143N MnSODs obtained from the DF/electrostatics method are –0.25, –0.29, and –0.11 V, which present the same trend and very similar relative values to those obtained from experimental kinetic rate constants (0.40, 0.32, and 0.59 V, respectively). The order $\Delta E_{redox}°$(human wild-type) < $\Delta E_{redox}°$(*T. thermophilus*) < $\Delta E_{redox}°$(*E. coli*) < $\Delta E_{redox}°$(Q143N) for MnSOD proteins is predicted by the DF/electrostatics calculations.

1. Introduction

Superoxide dismutases (SODs)[1] are a diverse group of metalloenzymes critical to the existence of oxygen-tolerant organisms. Their function is to dismute superoxide to molecular oxygen and hydrogen peroxide. In combination with the catalases which detoxify hydrogen peroxide (by conversion to molecular oxygen plus water), SODs form an important part of the biological defense against toxic oxygen intermediates and radical damage. Although their biological roles are not completely understood, SODs have been shown to prevent inflammation and oxidative damage and are involved in anticancer and antiaging mechanisms.[2−5]

Four types of SODs are known according to the redox-active metal involved: they are copper−zinc-, iron-, manganese-, and nickel-containing SODs.[6−9] MnSODs and FeSODs are normally grouped into one class because of their

* Corresponding authors. E-mail: lou@scripps.edu (L.N.) or wengehan@scripps.edu (W.-G.H.). Fax: (858) 784-8896.

(1) McCord, J. M.; Fridovich, I. *Free Radical Biol. Med.* **1988**, *5*, 363.
(2) Deng, H.-X.; Hentati, A.; Tainer, J. A.; Iqbal, Z.; Cayabyab, A.; Hung, W.-Y.; Getzoff, E. J.; Hu, P.; Herzfeldt, B.; Roos, R. P.; Wagner, C.; Deng, G.; Soriano, E.; Smith, C.; Parge, H. E.; Ahmed, A.; Roses, A. D.; Hallewell, R. A.; Pericak-Vance, M. A.; Siddique, T. *Science* **1993**, *261*, 1047.
(3) Fridovich, I. *Annu. Rev. Biochem.* **1995**, *64*, 97.
(4) Fridovich, I. *J. Biol. Chem.* **1997**, *272*, 18515.
(5) Miller, A.-F.; Sorkin, D. L. *Comments Mol. Cell. Biophys.* **1997**, *9*, 1.
(6) McCord, J. M.; Fridovich, I. *J. Biol. Chem.* **1969**, *244*, 6049.
(7) Yost, F. J.; Fridovich, I. *J. Biol. Chem.* **1976**, *248*, 4905.
(8) Keele, B. B., Jr.; McCord, J. M.; Fridovich, I. *J. Biol. Chem.* **1970**, *245*, 6176.
(9) Youn, H.-D.; Kim, E.-J.; Roe, J.-H.; Hah, Y. C.; Kang, S.-O. *Biochem. J.* **1996**, *318*, 889.

10.1021/ic010355z CCC: $22.00 © 2002 American Chemical Society
Published on Web 12/21/2001

identical set of coordinating ligands, similarities in sequence and protein structure, and similar catalytic pathways for superoxide dismutation. FeSODs are generally found in prokaryotes and plants, and MnSODs in prokaryotes and in the mitochondria of higher organisms (including humans). Because mitochondria use over 90% of the cell's oxygen, the mitochondrial electron transport chain produces a large quantity of oxygen radicals, and MnSOD is a primary biological defense against radical damage.[2−5,10−12]

All these enzymes function by dismuting the superoxide anion through the net reaction

$$2O_2^- + 2H^+ \rightarrow H_2O_2 + O_2 \quad (1)$$

In this paper, we will focus our study on the structural, energetic, pK_a, and redox potential properties of FeSODs and MnSODs (for previous density functional study on CuZnSOD, see ref 13). Several protein X-ray crystal structures have been determined for the Fe(Mn)SODs, for example, Fe(II)SOD and Fe(III)SOD from *Escherichia (E.) coli* at 1.8−1.85 Å resolution[14] and MnSODs from *Thermus (T.) thermophilus* at 1.8 Å (oxidized) and 2.3 Å (reduced),[15] from *E. coli* at 2.1 Å,[16] from human mitochondria wild-type at 2.2 Å (oxidized),[17] and from mutant Q143N at 2.3 Å (reduced).[18] All data confirm the structural similarities between MnSODs and FeSODs, especially within the first and second coordination shells surrounding the active site metal. The resting form of the SODs have active sites organized as approximate trigonal bipyramids with three histidines, one aspartate, and one hydroxyl (or water) ligand.

Letting "M" represent Mn or Fe, a general reaction scheme outlining the catalytic dismutation of superoxide ion (O_2^-) via alternating reduction of the M^{3+} and oxidation of the M^{2+} SOD enzyme is given here (ignoring protonation):[14,19,20]

$$M^{3+} + O_2^- \rightarrow M^{2+} + O_2 \quad (2)$$

$$M^{2+} + O_2^- \rightarrow M^{3+} + H_2O_2 \quad (3)$$

The actual reaction pathway is, however, more complicated. An inactive form of MnSOD has been observed to occur during the oxidative addition of O_2^- to the Mn(II) center. This inactive form slowly interconverts back to the active form.[21] On the basis of Michaelis−Menten kinetics, the inactive form only becomes relevant at high O_2^- concentrations. Several kinetics-based approaches have been employed to investigate the difference in catalytic properties between the various SODs, to characterize the inactive form of the complex between MnSOD and superoxide and to study the function of several important residues through comparing the catalytic properties of a wild-type SOD and its mutants.[18,21−25] Redox potentials have also been measured by spectroelectrochemistry using redox mediators for FeSOD and Fe-substituted MnSOD from *E. coli*[26] and for MnSODs from *E. coli* and *Bacillus (B.) stearothermophilus.*[27] From a historical perspective, the experimental measurement of redox potentials in SODs has been difficult.[28−30] The redox values measured depend greatly on the experimental conditions, for example, pH, nature of electrode, presence of a mediator, and the type of oxidizing/reducing agent used. Furthermore, the redox potential is actually a coupled redox process and corresponds to a one-electron redox event coupled with a single protonation or proton transfer.[31] In this paper, we present an approach to obtain the coupled redox potentials for Mn(Fe)SOD based on the standard experimental redox potential of the reaction ($O_2^- + 2H^+ + e^- \rightarrow H_2O_2$) and the measured kinetic rate constants of Mn(Fe)SOD. This scheme is a valuable and practical alternative to direct electrochemical measurements of redox potentials in SODs.

SODs have been the focus of much attention in our group for a number of years.[13,30,31] A set of methods to calculate their properties, that is, geometries, energies, pK_a's, and redox potentials, has been developed and is still being refined.[32−35] In our calculations on SODs, the active metal sites and nearby ligands are examined with quantum mechanical density functional (DF)[36] calculations. These quantum models are then embedded in an electrostatic/dielectric representation

(10) Land, W.; Zweier, J. L. *Transplant. Proc.* **1997**, *29*, 2567.
(11) Ambrosone, C. B.; Freudenheim, J. L.; Thompson, P. A.; Bowman, E.; Vena, J. E.; Marshall, J. R.; Graham, S.; Laughlin, R.; Nemoto, T.; Shields, P. G. *Cancer Res.* **1999**, *59*, 602.
(12) Mitrunen, K.; Silanpaa, P.; Kataja, V.; Eskelinen, M.; Kosma, V. M.; Benhamou, S.; Uusitupa, M.; Hirvonen, A. *Carcinogenesis* **2001**, *22*, 827.
(13) Konecny, R.; Li, J.; Fisher, C. L.; Dillet, V.; Bashford, D.; Noodleman, L. *Inorg. Chem.* **1999**, *38*, 940.
(14) Lah, M. S.; Dixon, M. M.; Pattridge, K. A.; Stallings, W. C.; Fee, J. A.; Ludwig, M. L. *Biochemistry* **1995**, *34*, 1646.
(15) Ludwig, M. L.; Metzger, A. L.; Pattridge, K. A.; Stallings, W. C. *J. Mol. Biol.* **1991**, *219*, 335.
(16) Edwards, R. A.; Baker, H. M.; Whittaker, M. M.; Whittaker, J. W.; Jameson, G. B.; Baker, E. N. *J. Biol. Inorg. Chem.* **1998**, *3*, 161.
(17) Borgstahl, G. E. O.; Parge, H. E.; Hickey, M. J.; Beyer, W. F.; Hallewell, R. A.; Tainer, J. A. *Cell* **1992**, *71*, 107.
(18) Hsieh, Y.; Guan, Y.; Tu, C.; Bratt, P. J.; Angerhofer, A.; Lepock, J. R.; Hickey, M. J.; Tainer, J. A.; Nick, H. S.; Silverman, D. N. *Biochemistry* **1998**, *37*, 4731.
(19) Lavelle, F.; McAdam, M. E.; Fielden, E. M.; Roberts, P. B.; Puget, K.; Michelson, A. M. *Biochem. J.* **1977**, *161*, 3.
(20) McAdam, M. E.; Fox, R. A.; Lavelle, F.; Fielden, E. M. *Biochem. J.* **1977**, *165*, 71.
(21) Bull, C.; Niederhoffer, E. C.; Yoshida, T.; Fee, J. A. *J. Am. Chem. Soc.* **1991**, *113*, 4069.
(22) Hsu, J.-L.; Hsieh, Y.; Tu, C.; O'Connor, D.; Nick, H. S.; Silverman, D. N. *J. Biol. Chem.* **1996**, *271*, 17687.
(23) Guan, Y.; Hickey, M. J.; Borgstahl, G. E. O.; Hallewell, R. A.; Lepock, J. R.; O'Connor, D.; Hsieh, Y.; Nick, H. S.; Silverman, D. N.; Tainer, J. A. *Biochemistry* **1998**, *37*, 4722.
(24) Hearn, A. S.; Tu, C.; Nick, H. S.; Silverman, D. N. *J. Biol. Chem.* **1999**, *274*, 24457.
(25) Cabelli, D. E.; Guan, Y.; Leveque, V.; Hearn, A. S.; Tainer, J. A.; Nick, H. S.; Silverman, D. N. *Biochemistry* **1999**, *38*, 11686.
(26) Vance, C. K.; Miller, A.-F. *J. Am. Chem. Soc.* **1998**, *120*, 461.
(27) Lawrence, G. D.; Sawyer, D. T. *Biochemistry* **1979**, *18*, 3045.
(28) Whittaker, J. W.; Whittaker, M. M. *J. Am. Chem. Soc.* **1991**, *113*, 5528.
(29) Verhagen, M. F. J. M.; Meussen, E. T. M.; Hagen, W. R. *Biochim. Biophys. Acta* **1995**, *1244*, 99.
(30) Fisher, C. L.; Chen, J.-L.; Li, J.; Bashford, D.; Noodleman, L. *J. Phys. Chem.* **1996**, *100*, 13498.
(31) Li, J.; Fisher, C. L.; Konecny, R.; Bashford, D.; Noodleman, L. *Inorg. Chem.* **1999**, *38*, 929.
(32) Chen, J.-L.; Noodleman, L.; Case, D. A.; Bashford, D. *J. Phys. Chem.* **1994**, *98*, 11059.
(33) Richardson, W. H.; Peng, C.; Bashford, D.; Noodleman, L.; Case, D. A. *Int. J. Quantum. Chem.* **1997**, *61*, 207.
(34) Li, J.; Fisher, C. L.; Chen, J.-L.; Bashford, D.; Noodleman, L. *Inorg. Chem.* **1996**, *35*, 4694.
(35) Li, J.; Nelson, M. R.; Peng, C. Y.; Bashford, D.; Noodleman, L. *J. Phys. Chem. A* **1998**, *102*, 6311.

of the remaining protein/solvent environment, and the energetics and other properties are then evaluated. In this paper, we will also use this DF/electrostatics scheme to calculate the coupled redox potentials for seven Mn(Fe)SOD structures. The results will be compared with the data obtained from reaction kinetics and from spectroelectrochemical redox potential measurements. The size of the active site clusters is increased (compared to our previous work[31]) and includes all second shell H-bonding components in the quantum mechanical DF calculations. Geometric properties of the various active site clusters in different oxidation states will also be discussed and compared with the X-ray crystallographic data.

Our paper is organized as follows: in section 2, we present our methodology for determining the coupled redox potential of Mn(Fe)SOD from the standard redox potential of reaction ($O_2^- + 2H^+ + e^- \rightarrow H_2O_2$) and the experimental kinetic rate constants. In section 3, we describe our active site cluster models. The method for the DF/electrostatics calculations is given in section 4. In section 5, we present and discuss our results, including structures, protonation properties for different metal oxidation states, possible proton-transfer reactions, pK_a's, and simple and coupled redox potentials. Finally, section 6 contains our conclusions.

2. Method for Deriving Mn(Fe)SOD Coupled Redox Potentials from Reaction Kinetics

The net reaction in eq 1 is the sum of the following two reactions:

$$O_2^- \rightarrow O_2 + e^- \tag{4}$$

$$O_2^- + 2H^+ + e^- \rightarrow H_2O_2 \tag{5}$$

Therefore, the standard free energy change of the net reaction $\Delta G°$(total) will be the sum of $\Delta G°$(4) and $\Delta G°$(5):

$$\Delta G°(\text{total}) = \Delta G°(4) + \Delta G°(5) \tag{6}$$

From the SOD X-ray crystallographic data alone, it is difficult to tell whether the fifth ligand coordinated to the metal (M) is a hydroxyl group (OH^-) or a water molecule (H_2O). Our earlier and present calculations show that $M^{3+}(OH^-)$ and $M^{2+}(H_2O)$ are the most stable forms for the oxidized and the reduced SOD active sites, respectively. We will present the evidence for this in section 5.2.1. Therefore, the actual redox potential that is measured in the protein and also that we calculate should be a coupled redox potential $\Delta E_{redox}°$(coupled), given by

$$M^{3+}(OH^-) + H^+ + e^- \rightarrow M^{2+}(H_2O) \tag{7}$$

We then have

$$\Delta E_{redox}°(\text{coupled}) = -\Delta G°(7) \tag{8}$$

Now, we rewrite eqs 2 and 3 in more detail as eqs 9 and 10, respectively, by including the coupled protonation (see Scheme 1 and also the discussion (especially Figure 9) in ref 14):

Scheme 1

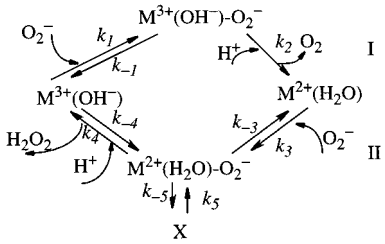

$$M^{3+}(OH^-) + O_2^- + H^+ \rightarrow M^{2+}(H_2O) + O_2 \tag{9}$$

$$M^{2+}(H_2O) + O_2^- + H^+ \rightarrow M^{3+}(OH^-) + H_2O_2 \tag{10}$$

Therefore,

$$\Delta G°(\text{total}) = \Delta G°(9) + \Delta G°(10) = \Delta G°(4) + \Delta G°(5) \tag{11}$$

Noting that eq 9 is the combination of eqs 4 and 7, we then have

$$\Delta G°(7) = \Delta G°(9) - \Delta G°(4) = \Delta G°(\text{total}) - \Delta G°(10) - \Delta G°(4) = \Delta G°(5) - \Delta G°(10) \tag{12}$$

The standard redox potential of eq 5 is known to be 0.89 V.[37,38] Therefore,

$$\Delta G°(5, \text{pH} = 7) = -\Delta E_{redox}°(5, \text{standard}) = -0.89 \text{ eV} \tag{13}$$

Now the key point is to evaluate $\Delta G°$(10) in eq 12, to obtain $\Delta E_{redox}°$(coupled) $= -\Delta G°$(7). We find $\Delta G°$(10) can be calculated from the kinetic rate constant results.

In Scheme 1, we see that the upper part (I) of the scheme represents reaction 9, and its lower half (II) represents reaction 10. "X" is the inactive form (dead-end intermediate) of Mn(II)SOD,[18,21−25] which is not found for FeSODs. The standard free energy change $\Delta G°$(II) in the second half process ($M^{2+}(H_2O) \rightarrow M^{3+}(OH^-)$) of Scheme 1 is exactly $\Delta G°$(10). From chemical kinetics theory, we have[39]

$$\Delta G°(10) = \Delta G°(\text{II}) = -RT\,[\ln(k_3/k_{-3}) + \ln(k_4/k_{-4})] \text{ (kcal/mol)} \tag{14}$$

where k_3, k_{-3}, k_4, and k_{-4} are the kinetic rate constants labeled in Scheme 1. T is the reaction temperature, and R is the molar gas constant. The kinetic rate constants have been measured for several MnSODs, for example, *T. thermophilus*,[21] human mitochondria wild-type,[22] and mutant Q143N.[18]

The kinetic parameters may be measured at pH_{exp} rather than pH = 7. The $\Delta G°$(5) at pH_{exp} will be

(36) Parr, R. G.; Yang, W. *Density Functional Theory of Atoms and Molecules*; Oxford University Press: New York, 1989.
(37) Holm, R. H.; Kennepohl, P.; Solomon, E. I. *Chem. Rev.* **1996**, *96*, 2239.
(38) Valentine, J. S. In *Bioinorganic Chemistry*; Bertini, I., Gray, H. B., Lippard, S. J., Valentine, J. S., Eds.; University Science Books: Mill Valley, CA, 1994; Chapter 5.
(39) Connor, K. A. *Chemical Kinetics: The Study of Reaction Rates in Solution*; VCR Publishers: New York, 1990; p 210.

$$\Delta G°(5, pH_{exp}) = -0.89 + [1.37 \times 2(pH_{exp} - 7)/23.06] \text{ (eV)} \quad (15)$$

where 23.06 is the conversion in units: 1 eV = 23.06 kcal/mol. From eqs 8, 12, 14, and 15, we now have

$$\Delta E_{redox}°(\text{coupled}, pH_{exp}) = -\Delta G°(5, pH_{exp}) + \Delta G°(10) = -[-0.89 + 1.37 \times 2(pH_{exp} - 7)/23.06] - RT[\ln(k_3/k_{-3}) + \ln(k_4/k_{-4})]/23.06 \quad (16)$$

Finally, we obtain the coupled redox potential of reaction 7 at pH = 7:

$$\Delta E_{redox}°(\text{coupled}, pH = 7) = \Delta E_{redox}°(\text{coupled}, pH_{exp}) + 1.37(pH_{exp} - 7)/23.06 \text{ (V)} \quad (17)$$

In the Results and Discussion section, we will present calculated values for coupled redox potentials using the above method. In the following section, we describe our active site cluster models and the combined DF/electrostatics methodology.

3. Protein Structures and Active Site Cluster Models

The different SOD proteins examined in this study include Fe(II)SOD (PDB Code: 1ISA) and Fe(III)SOD (1ISB) from *E. coli*,[14] MnSODs from *T. thermophilus* oxidized (PDB: 3MDS) and reduced,[15] from *E. coli* (PDB: 1VEW),[16] from human mitochondria (hMnSOD) wild-type (PDB: 1ABM)[17] and mutant Q143N (PDB: 1QNM).[18] The complete SOD protein is a tetramer, comprising two subunits related by a dyad axis. Each subunit consists of two chains (A and B), and each chain contains one metal active center. Similar to our previous work,[30,31] we use one subunit (chain A and B) of each protein in our calculations. The active site model for quantum DF calculations is taken from chain A, including also a single glutamate from chain B. The rest of chain A and chain B is treated as the protein environment.

Hydrogen atoms were added to the X-ray protein structures including structural water molecules, using the program package InsightII.[40] All the hydrogen atom positions were then optimized using cvff force field in InsightII with all heavy atoms fixed. All the active site models for different Mn(Fe)SODs were identical except for that of the Q143N mutant. A representative model of our active site (other than Q143N) is shown in Figure 1. We divided the active site into 13 parts. All the residues and linking atoms of the fragments labeled I−XIII in the active site model for different proteins are given in Table 1. I−V are the first shell ligands. Now, we use MnSOD from *T. thermophilus* as an example to describe the components in our active site model.

In this enzyme, the four protein side chain ligands bound to the Mn ion are His28, His83, His170, and Asp166 (labeled I, II, III, and IV in Figure 1, respectively). The methyl imidazole rings of His28 and His83 were extracted from the protein coordinates by breaking the $C_\beta-C_\alpha$ bond. To fill the open valence of atom C_β, a linking hydrogen atom[41,42] was added along the $C_\beta-C_\alpha$ vector (with bond length of 1.106 Å for $C_\beta-H_{link}$ in methyl group). The linking H atoms in this model lie at the junction between the quantum region and the classical region, and their coordinates in the whole active site cluster model were determined according to reasonable distances of C−H and N−H bonds (1.103 and 1.010 Å, respectively, in formamide). Label III denotes His170 and the main chain C═O group of Glu169. The atoms His170 C and Glu169 C_α are replaced by linking H atoms. Part IV represents an acetate anion taken from the side chain of Asp166. A water molecule or a hydroxyl group (OH^-) occupies the fifth ligand position surrounding the Mn ion, represented by V. M(H_2O) or M(OH^-) is used to specify whether the fifth ligand is H_2O or OH^-.

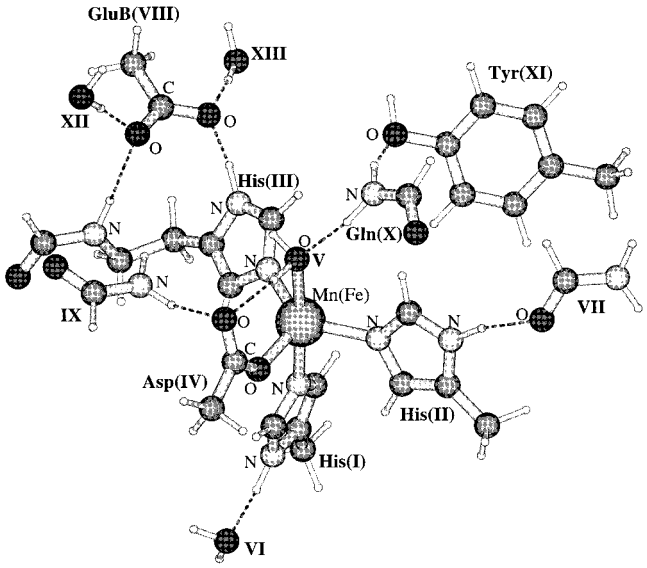

Figure 1. Quantum cluster active site model for wild-type Mn(Fe)SODs. The assignment of the various ligands (labeled I−XIII) from the different proteins is given in Table 1. Figure is generated with MOLDEN[67] and XFIG.[68]

The metal ion and the first shell ligands form a charged cluster which has strong H-bonding interactions with the surrounding protein side chain or backbone atoms. To describe the active site more accurately and include a greater part of the protein field quantum-mechanically, we include all second shell H-bonding fragments in the active site model. All the available protein X-ray data indicate a water molecule close to the nitrogen ($N_{\delta 1}$) of the histidine(I) (His28 here). This water molecule was then included as part VI in the active site. Part VII is a formamide which H-bonds to the $N_{\delta 1}-H$ group of His83 (II). The HC═O group of this formamide is taken from the Gly79 backbone, its NH_2 group from the backbone of His80, and two linking H atoms replace Gly79 C_α and His80 C_α. Part VIII is an acetate anion which corresponds to Glu169B (from chain B) and forms $O_{\epsilon 1}\cdots H-N$ and $O_{\epsilon 2}\cdots H_{\delta 1}-N_{\delta 1}$ H-bonds with His170 (III). Part IX is also a formamide (HC═O from Val167 and NH_2 main chain from Trp168) which H-bonds with Asp166 (IV) through the (Trp168)NH···(Asp166)$O_{\delta 1}$ interaction. Similar to VII, the atoms Val167 C_α and Trp168 C_α are replaced

(40) *Insight II User Guide*; San Diego, CA, 1995.
(41) Han, W.-G.; Tajkhorshid, E.; Suhai, S. *J. Biomol. Struct. Dyn.* **1999**, *16*, 1019.
(42) Field, M. J.; Bash, P. A.; Karplus, M. *J. Comput. Chem.* **1990**, *11*, 700.

Table 1. Components of the Active Site Models[a]

		FeSOD	MnSOD		
source		*E. coli*	*T. thermophilus*	*E. coli*	human mitochondria
PDB code		1ISA (red.) 1ISB (ox.)	*T.T.* (red.)[b] 3MDS (ox.)	1VEW	1ABM (wild, ox.) 1QNM (Q143N, red.)
I	res.	His26	His28	His26	His26
	link	His26 C_α	His28 C_α	His26 C_α	His26 C_α
II	res.	His73	His83	His81	His74
	link	His73 C_α	His83 C_α	His81 C_α	His74 C_α
III	res.	His160 Glu159	His170 Glu169	His171 Glu170	His163 Glu162
	link	His160 C, Glu159 C_α	His170 C, Glu169 C_α	His171 C, Glu170 C_α	His163 C, Glu162 C_α
IV	res.	Asp156	Asp166	Asp167	Asp159
	link	Asp156 C_α	Asp166 C_α	Asp167 C_α	Asp159 C_α
V	res.	HOH194	HOH205	HOH207	HOH200
VI	res.	HOH443 (red.) HOH440 (ox.)	HOH260 (red.) HOH213 (ox.)	HOH261	HOH266 (wild) HOH52 (Q143N)
VII	res.	Gln69 Val70	Gly79 His80	Gly77 His78	Gly70 His71
	link	Gln69 C_α, Val70 C_α	Gly79 C_α, His80 C_α	Gly77 C_α, His78 C_α	Gly70 C_α, His71 C_α
VIII	res.	Glu159B[c]	Glu169B	Glu170B	Glu162B
	link	Glu159B C_β	Glu169B C_β	Glu170B C_β	Glu162B C_β
IX	res.	Val157 Trp158	Val167 Trp168	Val168 Trp169	Val160 Trp161
	link	Val157 C_α, Trp158 C_α	Val167 C_α, Trp168 C_α	Val168 C_α, Trp169 C_α	Val160 C_α, Trp161 C_α
X	res.	Gln69	Gln151	Gln146	Gln143 (wild) Asn143 (Q143N)
	link	Gln69 C_γ	Gln151 C_γ	Gln146 C_γ	Gln 143 C_γ, Asn143 C_β
XI	res.	Tyr34	Tyr36	Tyr34	Tyr34
	link	Tyr34 C_α	Tyr34 C_α	Tyr34 C_α	Tyr34 C_α
XII	res.	HOH434 (red.) HOH436 (ox.)	HOH261 (red.) HOH270 (ox.)	HOH1261	HOH302 (wild) HOH37 (Q143N)
XIII	res.	HOH419 (red.) HOH421 (ox.)	HOH238 (red.) HOH328B (ox.)	HOH1731B	HOH207 (wild) HOH353 (Q143N)
XIV	res.				HOH88 (Q143N)

[a] Labels I−XIV are shown in Figures 1 and 2; red. = reduced, ox. = oxidized, res. = residue(s), and link = linking atom(s). [b] The reduced MnSOD crystal structure (*T.T.* (red.)) of *Thermus thermophilus* was obtained directly from M. L. Ludwig's group.[15] [c] The acetate anion group is taken from Glu of chain B (e.g., Glu159B for FeSOD). All other groups are taken from chain A by default.

with linking H atoms. Part X is also a formamide which represents the side chain of Gln151 capable of H-bonding with the H_2O or OH^- of site V through $N_{\epsilon 2}H_{\epsilon 22}\cdots O(V)$ interaction. Another hydrogen $H_{\epsilon 21}$ bonded to $N_{\epsilon 2}$ in Gln151 also H-bonds with the oxygen atom on the phenyl group of Tyr36 (XI) and is therefore included as methyl phenol (part XI) to represent Tyr36. The H-bonding network between the bound OH^- (or H_2O), Gln(X), and Tyr(XI) is believed to play an important role in proton-transfer reactions during the catalytic cycle.[9,14,31] Gln(X) is conserved in the majority of the known MnSODs and in some bacterial forms of the enzyme, and Tyr(XI) is conserved in all of the MnSODs reported to date and in the FeSODs as well.[18]

XII and XIII are two water molecules which have strong H-bonding interactions with the carboxylate group of Glu169B (part VIII). We noticed that, in all of the Mn(Fe)SOD crystal structures, there exist at least two water molecules within H-bonding distances with the two oxygen atoms of the Glu169B carboxylate group. The closest two water molecules were included in the active site model cluster for each protein. Without these water molecules, the proton $H_{\delta 1}$ on $N_{\delta 1}$ of His170 (part III) would transfer to $O_{\epsilon 2}$ of Glu169B (part VIII) during the DF geometry optimization calculations. These water molecules certainly play an important role in governing the electron distribution and, therefore, also influence the electronic potential around the carboxylate group of Glu169B (part VIII).

The active site of Q143N hMnSOD is significantly different from those of the wild-type Mn(Fe)SOD proteins. Because, in Q143N, the Gln143 (part X, in the wild-type hMnSOD) is replaced by Asn143, the distance between the side chain terminal amide and the H_2O or OH^- ligand on site V increases. From the Q143N crystallographic data, a new water molecule (HOH88 in chain A) fills the cavity created by the Gln143 → Asn mutation.[18] In chain A of Q143N, the side chain OH of Tyr34 (part XI) is pushed away 0.9 Å by this new water molecule and, hence, no longer forms a direct H-bond with the side chain of Asn143. Both Tyr34 and Asn143 are now H-bonded to the new water molecule, which also H-bonds to the original H_2O or OH^- ligand. The relative positions of this new water molecule and the side chain of Asn143 and Tyr34 are shown as part XIV, X, and XI, respectively, in Figure 2. Other aspects of the structure in the active site cluster of Q143N are the same as those of the wild-type Mn(Fe)SODs shown in Figure 1.

In our calculations, the starting geometries of the active site cluster models for different proteins were built up from the original crystal structure data, while the final geometries for both reduced and oxidized states in H_2O or OH^- bound forms were obtained by the density functional (DF) geometry optimization calculations with some backbone atoms and all linking atom positions fixed. The final energetic properties were computed by including the electrostatic/dielectric solvation effects. The detailed computational method is described in the next section.

4. DF/Electrostatics Computational Methodology

All quantum mechanical DF calculations have been performed using the Amsterdam Density Functional (ADF, Version 2.3)

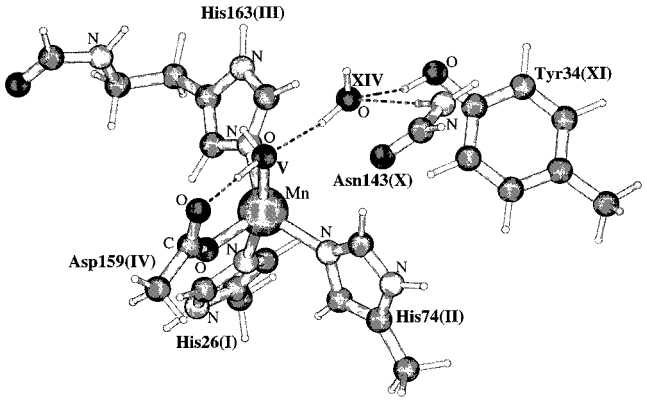

Figure 2. The principal differences between the active site model of mutant Q143N human MnSOD and the wild-type Mn(Fe)SODs are shown. After the replacement of Gln143 → Asn in Q143N, an extra water molecule (labeled as XIV) appears in the active site and is H-bonded with the original H_2O or OH^- ligand (on site V) and both Tyr34 (XI) and Asn143 (X) side chains. Figure is generated with MOLDEN[67] and XFIG.[68]

package.[43−46] The parametrization of Vosko, Wilk, and Nusair (VWN)[47] was used for the local density approximation term, and the corrections of Becke(1988) (B)[48] and Perdew(1986) (P)[49] were used for the nonlocal exchange and correlation terms. We designate this VWN-BP method as VBP hereafter. The molecular orbitals were expanded in an uncontracted triple-ζ Slater-type orbital (STO) basis set, along with a single set of polarization functions, which constitutes basis set IV in the ADF code. The inner core shells of C(1s), N(1s), O(1s), and Mn(Fe)(1s,2s,2p) were treated by the frozen core approximation. The accuracy parameter (accint) for the numerical integration grid was set to 4.0. The spin-unrestricted method was used for all density functional calculations.

To obtain coupled redox potentials and to see whether a H_2O or OH^- is bound to the reduced and oxidized metal centers, for each protein, we performed VBP geometry optimization calculations on four kinds of active site structures, that is, $M^{3+}(H_2O)$, $M^{3+}(OH^-)$, $M^{2+}(H_2O)$, and $M^{2+}(OH^-)$. The positions of all linking H atoms, the backbone atoms except for nitrogen of part III, the C═O or N−H groups of formamide which do not have H-bonding interactions, and the oxygen positions of water XII and XIII were fixed during our calculations.

Following geometry optimization, a modified version of CHELPG code[50,51] was used to fit the point charges from the molecular electrostatic potentials (ESP) calculated by ADF. The singular value decomposition (SVD) method[51] was introduced into the code to minimize the uncertainties in the fitting procedure. The total net charge and the three Cartesian dipole moment components of each cluster were used as constraint conditions for the fit. Our quantum clusters $M^{3+}(OH^-)$, $M^{3+}(H_2O)$, $M^{2+}(OH^-)$, and $M^{2+}(H_2O)$ have net charges of 0, 1, −1, and 0, respectively. The fitted points lay on a cubic grid between the van der Waals radius and the outer atomic radius with a grid spacing of 0.2 Å. The outer atomic radius (5.0 Å here for all atoms) defines the outer boundary of the electrostatic potential that is used in the charge fitting. The van der Waals radii for C, O, N, H, Mn, and Fe were 1.67, 1.4, 1.55, 1.2, 1.5, and 1.5 Å, respectively. To keep charge conservation and to avoid unphysical charge interactions, the charges of all linking H atoms were set to zero, but these atoms were included in constructing the fitting grid envelope.

Using the MEAD (Macroscopic Electrostatics with Atomic Detail) program suite developed by Bashford,[52,53] we performed the protein/reaction field energy (E_{pr}) calculations.[31,32,35,51,54,55] In this approach, the solute and the protein field are represented by a set of atomic charges and Born radii with dielectric constant $\epsilon = 1$ and $\epsilon = 4$, respectively, and solvent (water) as a continuous dielectric medium (with $\epsilon = 80$). The MEAD program solves the Poisson−Boltzmann equation using a numerical finite-difference method. The protein field interaction energy E_p is obtained from the electrostatic potential of all the protein charges (screened by the protein and solvent dielectric media) acting on the ESP charges of the active site quantum cluster. On the other hand, the reaction field energy E_r is generated by the active site cluster charges which polarize the protein and solvent dielectrics. This polarization potential acts back on the active site cluster charges. As in our previous work,[31] Born radii of 1.50 ($Mn^{2+/3+}$, $Fe^{2+/3+}$), 1.55 (N), 1.67 (C), 1.40 (O), and 1.20 (H) Å were used for the active site atoms, and the PARSE[56] radii and charges were assigned to atoms in the protein field. Considering that the active site metal center of chain B can be in either the oxidized or reduced state, and the PARSE charges do not describe either properly with sufficient accuracy, the ESP charges of the optimized $M^{3+}(OH^-)$ and M^{2+}-(H_2O) clusters were used to represent the oxidized and reduced states of the metal clusters in chain B, respectively. When defining the dielectric boundaries, the linking carbon atoms (see Table 1) were included in both the active site and protein field regions.[35] The charges of these linking carbon atoms were set to zero in the active site clusters. The dielectric boundary between the interior (with $\epsilon = 1$) and the exterior of the active site region is then defined by the contact surface of rolling a probe sphere (with radius $r = 1.4$ Å) over the "quantum cluster plus linking carbon atoms" region.[31,57] A similar procedure is then used to distinguish the protein region ($\epsilon = 4$) from the solvent region ($\epsilon = 80$).

Next, we describe how to calculate the coupled redox potential of reaction 7 on the basis of our combined DF/electrostatics calculations.

Let $E[M(H_2O)]$ be the DF energy of active site cluster $M(H_2O)$ from VBP calculations, and $E_{pr} = (E_p + E_r)$ be the sum of its protein and reaction field energies. The simple redox potential on going from $M^{3+}(H_2O)$ to $M^{2+}(H_2O)$ in MSOD is calculated from

$$\Delta E_{redox}°[M(H_2O)] = \{E[M^{3+}(H_2O)] - E[M^{2+}(H_2O)]\} + \{E_{pr}[M^{3+}(H_2O)] - E_{pr}[M^{2+}(H_2O)]\} + \Delta SHE = IP_{red} + \Delta E_{pr}(redox) - 4.43\ (V) \quad (18)$$

where IP_{red} is the gas-phase ionization potential of the reduced cluster and $\Delta SHE = -4.43$ V is the standard hydrogen electrode

(43) *ADF 2.3.0*; Theoretical Chemistry, Vrije Universiteit: Amsterdam.
(44) Baerends, E. J.; Ellis, D. E.; Ros, P. *Chem. Phys.* **1973**, *2*, 41.
(45) te Velde, G.; Baerends, E. J. *J. Comput. Phys.* **1992**, *99*, 84.
(46) Guerra, C. F.; Visser, O.; Snijders, J. G.; te Velde, G.; Baerends, E. J. In *Methods and Techniques for Computational Chemistry*; Clementi, E., Corongiu, G., Eds.; STEF: Cagliari, Italy, 1995; p 305.
(47) Vosko, S. H.; Wilk, L.; Nusair, M. *Can. J. Phys.* **1980**, *58*, 1200.
(48) Becke, A. D. *Phys. Rev. A* **1988**, *38*, 3098.
(49) Perdew, J. P. *Phys. Rev. B* **1986**, *33*, 8822; **1986**, *34*, 7406 (erratum).
(50) Breneman, C. M.; Wiberg, K. B. *J. Comput. Chem.* **1990**, *11*, 361.
(51) Mouesca, J.-M.; Chen, J. L.; Noodleman, L.; Bashford, D.; Case, D. A. *J. Am. Chem. Soc.* **1994**, *116*, 11898.
(52) Bashford, D.; Gerwert, K. *J. Mol. Biol.* **1992**, *224*, 473.
(53) Bashford, D. In *Scientific Computing in Object-Oriented Parallel Environments*; Ishikawa, Y., Oldehoeft, R. R., Reynders, J. V. W., Tholburn, M., Eds.; Lecture Notes in Computer Science; Springer: Berlin, 1997; Vol. 1343, p 233.
(54) Bashford, D.; Karplus, M. *Biochemistry* **1990**, *29*, 10219.
(55) Lim, C.; Bashford, D.; Karplus, M. *J. Phys. Chem.* **1991**, *95*, 5610.
(56) Sitkoff, D.; Sharp, K. A.; Honig, B. *J. Phys. Chem.* **1994**, *98*, 1978.
(57) Richards, F. M. *Annu. Rev. Biophys. Bioeng.* **1977**, *6*, 151.

potential.[58] Similarly, the simple redox potential $\Delta E_{redox}°[M(OH^-)]$ on going from $M^{3+}(OH^-)$ to $M^{2+}(OH^-)$ can be calculated in the same way.

To calculate the coupled redox potential of reaction 7, we also need to know the pK_a value of the active site for the $M^{2+}(H_2O)$ form. The pK_a values also provide information regarding the likely protonation state of the SOD active site. In general, the pK_a value of the $M^{2+/3+}(H_2O)$ clusters can be obtained as[31]

$$1.37pK_a[M^{2+/3+}(H_2O)] = \{E[M^{2+/3+}(OH^-)] + E[H^+] - E[M^{2+/3+}(H_2O)]\} + \{E_{pr}[M^{2+/3+}(OH^-)] - E_{pr}[M^{2+/3+}(H_2O)]\} - 268.26 + E_{corr} = PA + \Delta E_{pr}(\text{deproton}) - 268.26 \quad (19)$$

where $E[H^+] = 12.6523$ eV is the calculated ionization energy of a spin restricted H atom obtained from DF calculation; E_{corr} is a correction term to the proton affinity PA, including zero point energy (ΔZPE) and 5/2RT work.[59] As in our previous calculations, we use $\Delta ZPE = -7.1$ and -7.7 kcal/mol for $Mn^{2+}(Fe^{2+})$ and $Mn^{3+}(Fe^{3+})$ clusters, respectively.[31] The value -268.26 kcal/mol is the sum of the solvation free energy of a proton (-260.5 kcal/mol)[60] and the entropic portion of the gas-phase free energy of a proton ($-T\Delta S_{gas}(H^+) = -7.76$ kcal/mol at 298 K and 1 atm pressure).[59]

Finally, the coupled redox potential of MSOD for reaction 7 at pH = 7 can be obtained:[31]

$$\Delta E_{redox}°(\text{coupled, pH} = 7) = \Delta E_{redox}°[M(OH^-)] + 1.37\{pK_a[M^{2+}(H_2O)] - 7.0\}/23.06 \quad (20)$$

The coupled redox potentials calculated from eq 20 will be compared with experimental values obtained by direct redox measurements or from analysis of kinetics measurements using eqs 16 and 17.

5. Results and Discussion

5.1. Coupled Redox Potentials from Reaction Kinetics. On the basis of the method described in section 2, the coupled redox potentials $\Delta E_{redox}°$(coupled, pH = 7) of 0.40, 0.31, and 0.58 V have been obtained for MnSODs from *T. thermophilus*,[21] human mitochondria wild type,[22] and mutant Q143N,[18] respectively. The experimental pH values (pH_{exp}), temperature (T), kinetic rate constants in Scheme 1, and the final coupled redox potentials derived from eqs 16 and 17 at both pH_{exp} and pH = 7 are given in Table 2.

The coupled redox potential of the Q143N mutant is 0.27 V higher than that of the wild-type hMnSOD, which supports the conclusion from the kinetics experiments that the Gln143 → Asn mutation increases the reduction potential of manganese to stabilize the Mn(II) form, indicating that Gln143 has a substantial role in maintaining a reduction potential favorable for the oxidation and reduction halves of the catalytic cycle.[18]

As far as we know, there are only three direct redox potential measurements for Mn(Fe)SODs. One is for *E. coli* FeSOD (0.223 V at pH = 7.4);[26] the other two were measured in 1979 for MnSOD from *B. stearothermophilus* and *E. coli* (0.26 and 0.31 V, respectively, at pH = 7).[27] The method we have proposed on the basis of kinetic rate constants provides a useful alternative and also a cross-check on the direct redox results (once the latter are obtained in the same systems). It is apparent from the law of mass action, eqs 9,10,14−17, and Scheme 1, that the driving force for the reaction can be controlled by pH, with higher pH corresponding to less driving force, thereby facilitating the kinetic measurements (Table 2) and observations of the pH dependence of the redox potential. Quantitatively, the kinetic scheme may change at very high pH (≥9) where the complication of another OH^- binding competitively to the open coordination site in the M^{3+} metal center may occur.[14]

Table 2. Coupled Redox Potentials Obtained from Reaction Kinetics[a]

	MnSOD		
	T. thermophilus[b]	human wild type[c]	human Q143N[d]
pH_{exp}	9.3	9.4	9.4
T (K)	275	293	278
k_1 (M^{-1} s^{-1})	1.5×10^9	2×10^9	2×10^9
k_{-1} (s^{-1})	3.5×10^4	2×10^4	1.5×10^6
k_2 (s^{-1})	2.5×10^4	8×10^4	6×10^2
k_3 (M^{-1} s^{-1})	1.5×10^9	2×10^9	2×10^9
k_{-3} (s^{-1})	3.5×10^4	2×10^4	1.5×10^6
k_4 (s^{-1})	2.5×10^4	8×10^4	6×10^2
k_{-4} (M^{-1} s^{-1})	3×10^2	3×10^2	1×10^3
$\Delta G°(10)$ (eV)[e]	−0.36	−0.43	−0.16
$\Delta G°(5, pH_{exp})$ (eV)[f]	−0.62	−0.60	−0.60
$\Delta E_{redox}°$(coupled, pH_{exp}) (V)[g]	0.26	0.17	0.44
$\Delta E_{redox}°$(coupled, pH = 7) (V)[h]	0.40	0.31	0.58

[a] Calculations are based on the method described in section 2. [b] Kinetic rate constants from ref 21. [c] Kinetic rate constants from ref 22. [d] Kinetic rate constants from ref 18. [e] From eq 14. [f] From eq 15. [g] From eq 16. [h] From eq 17.

5.2. Results from DF/Electrostatics Calculations. In addition to coupled redox potentials, we are also interested in the structures, energies, and protonation properties of the active site clusters with different oxidation states. Furthermore, from the geometrical character of the active site clusters and the catalytic kinetic properties, we would like to gain insight into the proton-transfer process during the first half of the cycle in Scheme 1.

In Table 3, we present the metal−ligand (first shell) and some second shell H-bonding distances from the crystal structures of the Mn(Fe)SODs studied. All metal−N(His I−III) bond lengths are quite similar (around 2.1 Å) in the proteins other than wild-type hMnSOD, where the distances of Mn−N(His I−III) in both chain A and chain B are very short (∼1.505−1.625 Å).[61] The suggested oxidation states derived from the original references are also given in Table 3.[14−18] The principal difficulty in the interpretation of the structural data arises because of uncertainties in oxidation states of the proteins and whether pure oxidation states or mixed states are present. Edwards et al. have suggested that their MnSOD structure from *E. coli* is a mixture having both Mn^{3+} and Mn^{2+} moieties.[16] In wild-type hMnSOD, the two

(58) Reiss, H.; Heller, A. *J. Phys. Chem.* **1985**, *89*, 4207.
(59) Tawa, G. J.; Topol, I. A.; Burt, S. K.; Caldwell, R. A.; Rashin, A. A. *J. Chem. Phys.* **1998**, *109*, 4852.
(60) Noyes, R. M. *J. Am. Chem. Soc.* **1962**, *84*, 512.
(61) Stroupe, E.; Tainer, J. A. Private communication. The distances of Mn−N(His I−III) in PDB file 1ABM for wild-type hMnSOD are known to be incorrect. The actual distances are around 2.1 Å as stated in ref 17. Further modeling and refinement of this structure is underway.

Table 3. Geometries (Å) of MSOD Active Site Clusters in Their Crystal Structures[a]

source	FeSOD				MnSOD									
	E. coli[b]				*T. thermophilus*[c]				*E. coli*[d]		*human mitochondria*			
PDB code	1ISA (red.)		1ISB (ox.)		*T.T.* (red.)		3MDS (ox.)		1VEW		1ABM[e] (wild, ox.)		1QNM[f] (Q143N, red.)	
chain	A	B	A	B	A	B	A	B	A	B	A	B	A	B
M−N(I)	2.186	2.186	2.153	2.172	2.090	2.176	2.138	2.138	2.146	2.093	1.625	1.546	2.283	2.126
M−N(II)	2.063	2.027	2.061	2.030	2.135	2.098	2.115	2.080	2.222	2.206	1.508	1.545	2.149	2.162
M−N(III)	2.125	2.115	2.078	2.061	2.180	2.233	2.152	2.177	2.161	2.168	1.505	1.593	2.294	2.123
M−O(IV)	1.953	1.924	1.889	1.931	1.828	1.842	1.803	1.786	2.011	2.028	2.074	2.211	1.926	2.115
M−O(V)	2.026	2.061	1.920	1.997	2.227	2.242	2.072	2.090	2.159	2.181	2.103	1.702	2.259	2.136
O(IV)···O(V)	2.789	2.796	3.028	2.897	2.735	2.559	2.824	2.730	2.806	2.726	2.763	2.696	2.724	3.015
O(IV)···N(IX)	3.167	3.210	3.199	3.104	3.117	3.115	3.173	3.143	3.223	3.185	2.986	3.150	3.067	3.099
O(V)···N(X)	3.423	3.414	3.485	3.331	3.095	3.056	3.011	2.970	2.919	3.016	3.235	3.537		
N(X)···O(XI)	3.110	3.114	3.098	3.176	2.909	2.854	3.108	2.915	3.001	3.036	2.683	2.853		
O(V)···O(XIV)													2.691	2.740
O(XIV)···N(X)													2.983	2.557
O(XIV)···O(XI)													2.462	2.450

[a] Labels I−XIV are shown in Figures 1 and 2. M = Fe or Mn ion, red. = reduced, ox. = oxidized. The oxidation states were suggested by the original references. [b] Ref 14. [c] From ref 15. Also see footnote *b* of table 1. [d] Ref 16. [e] Ref 17. Also see ref 61. [f] Ref 18.

Table 4. Geometries (Å) and Energies (eV) of the Optimized $M^{3+}(OH^-)$ Active Site Clusters[a]

	FeSOD		MnSOD				
starting geometry:	1ISA	1ISB	*T.T.* (red.)[b]	3MDS	1VEW	1ABM	1QNM
M−N(I)	2.320	2.315	2.102	2.095	2.103	2.088	2.096
M−N(II)	2.101	2.105	2.106	2.114	2.138	2.095	2.139
M−N(III)	2.087	2.084	2.052	2.056	2.086	2.045	2.065
M−O(IV)	1.965	1.945	2.001	2.010	2.021	1.997	2.012
M−O(V)	1.859	1.868	1.810	1.809	1.808	1.814	1.809
O(IV)···O(V)	2.776	2.905	2.787	2.764	2.751	2.850	2.684
O(IV)···N(IX)	3.315	3.261	3.216	3.220	3.427	3.314	3.450
O(V)···N(X)	3.456	3.432	3.053	3.066	3.036	3.182	
O(V)···O(XIV)							2.619
O(XIV)···N(X)							3.131
O(XIV)···O(XI)							2.685
$E[M^{3+}(OH^-)]$[c]	−613.8275	−613.7585	−615.2931	−615.6084	−615.8300	−615.8756	−630.2020
E_{pr}(III)[d]	−3.6281	−3.6115	−3.8869	−3.6554	−3.5774	−3.5129	−3.5944
E_{pr}(II)[d]	−3.6315	−3.6091	−3.8904	−3.6587	−3.5836	−3.5146	−3.5934

[a] Optimized geometries were obtained from density functional VBP calculations. M = Fe or Mn ion. Labels I−XIV are shown in Figures 1 and 2. [b] See footnote *b* of Table 1. [c] Quantum mechanical VBP energy (with respect to a reference state formed by the sum of spin restricted atom energies for the atoms of the clusters). [d] The sum of protein field and reaction field solvation energies. E_{pr}(III) and E_{pr}(II) were obtained by treating the active site of chain B as $M^{3+}(OH^-)$ and $M^{2+}(H_2O)$, respectively.

Mn−O(V) distances are very different in chain A (2.103 Å) and in chain B (1.702 Å), perhaps a direct consequence of different oxidation and protonation states of the two Mn centers. Possibly, the active site of chain A has the Mn^{2+}-(H_2O) form present and chain B is in the $Mn^{3+}(OH^-)$ form. Most likely, there is a distribution of $Mn^{3+}(OH^-)$ and Mn^{2+}-(H_2O) sites throughout the crystal in both the A and B chains. Because of fluctuations associated with the atomic positions, there are intrinsic uncertainties and errors associated with using the bond distances and angles of the experimental data. Therefore, the active-site structures (taken from chain A) are geometry optimized to give more accurate and comparable quantum mechanical energies.

5.2.1. Oxidation and Protonation States and Possible Proton Transfers in Catalytic Reactions Predicted from the Structural and Energetic Properties of the Optimized Clusters. The main bond lengths and electronic and solvation energies of our optimized $M^{3+}(OH^-)$, $M^{3+}(H_2O)$, $M^{2+}(OH^-)$, and $M^{2+}(H_2O)$ clusters are given in Tables 4, 5, 6, and 7, respectively. Two kinds of protein and reaction field energies E_{pr} were calculated for each cluster. The energies E_{pr}(III) and E_{pr}(II) were obtained by treating the active site of chain B as $M^{3+}(OH^-)$ and $M^{2+}(H_2O)$, respectively (see section 4).

Because the initial crystal structures differ from the outset, and specific atomic positions are fixed during geometry optimization, the final optimized structures also differ within each protein data set. The originally very short Mn−N(His I−III) distances in the wild-type hMnSOD crystal structure 1ABM are now elongated to more than 2.0 Å in the four possible active site clusters and are very similar to the corresponding bond lengths of other MnSOD structures.

In the starting geometries of the $M^{3+}(H_2O)$ clusters, one of the protons of the water molecule on site V H-bonds with the atom $O_{\delta 1}$ of the aspartate on site IV. During geometry optimization processes of all $Mn^{3+}(H_2O)$ clusters, this proton gradually moved closer to the atom $O_{\delta 1}$ and finally transferred to $O_{\delta 1}$. Meanwhile, it remained H-bonded with the oxygen atom of the original water molecule (V). For instance, the bond length $r(H-O_{\delta 1}(IV)) = 1.037$ Å and $r(H\cdots O(V)) = 1.619$ Å in the optimized $Mn^{3+}(H_2O)$, starting from the crystal structure of 3MDS. Therefore, the oxidized Mn^{3+} center prefers a OH^- group rather than a water

Table 5. Geometries (Å) and Energies (eV) of the Optimized $M^{3+}(H_2O)$ Active Site Clusters[a]

	FeSOD		MnSOD				
starting geometry:	1ISA	1ISB	*T.T.* (red.)[b]	3MDS	1VEW	1ABM	1QNM
M−N(I)	2.144	2.151	2.077	2.047	2.082	2.072	2.097
M−N(II)	2.041	2.050	2.078	2.068	2.087	2.085	2.113
M−N(III)	2.094	2.081	2.035	2.029	2.077	2.049	2.075
M−O(IV)	1.969	1.950	2.129	2.157	2.182	2.145	2.151
M−O(V)	2.207	2.195	1.909	1.889	1.928	1.907	1.958
O(IV)···O(V)	2.570	2.557	2.617	2.642	2.613	2.614	2.563
O(IV)···N(IX)	3.377	3.500	3.675	3.876	3.850	3.789	3.801
O(V)···N(X)	3.563	3.652	3.163	3.118	3.076	3.380	
O(V)···O(XIV)							2.778
O(XIV)···N(X)							3.228
O(XIV)···O(XI)							2.762
$E[M^{3+}(H_2O)]$[c]	−611.9722	−611.9136	−613.0944	−613.3402	−613.6370	−613.7303	−628.0812
E_{pr}(III)[d]	−3.8158	−3.7616	−4.3154	−4.3121	−3.8955	−3.7977	−3.7848
E_{pr}(II)[d]	−3.7594	−3.7057	−4.2685	−4.3593	−3.8962	−3.7992	−3.7843

[a−d] See notations under Table 4.

Table 6. Geometries (Å) and Energies (eV) of the Optimized $M^{2+}(OH^-)$ Active Site Clusters[a]

	FeSOD		MnSOD				
starting geometry:	1ISA	1ISB	*T.T.* (red.)[b]	3MDS	1VEW	1ABM	1QNM
M−N(I)	2.626	2.600	2.451	2.397	2.443	2.509	2.352
M−N(II)	2.126	2.143	2.180	2.204	2.233	2.193	2.197
M−N(III)	2.120	2.117	2.148	2.135	2.180	2.145	2.150
M−O(IV)	2.041	2.046	2.067	2.080	2.072	2.040	2.045
M−O(V)	1.973	1.978	2.019	2.009	2.019	2.029	2.120
O(IV)···O(V)	3.524	3.646	3.379	3.215	3.296	3.523	3.260
O(IV)···N(IX)	2.888	2.832	2.866	3.018	3.016	2.972	3.028
O(V)···N(X)	2.920	3.006	2.616	2.671	2.629	2.645	
O(V)···O(XIV)							2.482
O(XIV)···N(X)							2.867
O(XIV)···O(XI)							2.511
$E[M^{2+}(OH^-)]$[c]	−616.3885	−616.2797	−617.5694	−617.8468	−618.4233	−618.2218	−633.1151
E_{pr}(III)[d]	−4.8805	−4.8205	−5.2171	−4.8935	−4.8158	−4.7474	−4.8281
E_{pr}(II)[d]	−4.8591	−4.8479	−5.1853	−4.9369	−4.8193	−4.7491	−4.8267

[a−d] See notations under Table 4.

Table 7. Geometries (Å) and Energies (eV) of the Optimized $M^{2+}(H_2O)$ Active Site Clusters[a]

	FeSOD		MnSOD				
starting geometry:	1ISA	1ISB	*T.T.* (red.)[b]	3MDS	1VEW	1ABM	1QNM
M−N(I)	2.200	2.192	2.215	2.192	2.216	2.242	2.223
M−N(II)	2.074	2.085	2.119	2.132	2.153	2.125	2.149
M−N(III)	2.088	2.091	2.131	2.139	2.164	2.130	2.154
M−O(IV)	2.001	2.001	2.065	2.086	2.095	2.041	2.071
M−O(V)	2.323	2.315	2.311	2.286	2.304	2.320	2.324
O(IV)···O(V)	2.613	2.627	2.575	2.543	2.537	2.573	2.524
O(IV)···N(IX)	3.327	3.374	3.267	3.412	3.600	3.527	3.590
O(V)···N(X)	3.467	3.571	3.069	3.041	2.917	3.212	
O(V)···O(XIV)							2.726
O(XIV)···N(X)							3.129
O(XIV)···O(XI)							2.748
$E[M^{2+}(H_2O)]$[c]	−618.0651	−618.0214	−619.1474	−619.4551	−619.7569	−619.7376	−634.2047
E_{pr}(III)[d]	−3.5976	−3.5977	−3.8530	−3.6322	−3.5538	−3.4307	−3.5522
E_{pr}(II)[d]	−3.6007	−3.5957	−3.8566	−3.6348	−3.5557	−3.4321	−3.5509

[a−d] See notations under Table 4.

molecule on the fifth binding site. The resting state oxidized M^{3+}SODs are, therefore, in the $M^{3+}(OH^-)$ forms. In a subsequent section, our pK_a calculations will further support this conclusion for both Mn−SOD and Fe−SOD systems.

Next, we examine the structures of the optimized $M^{2+}(OH^-)$ clusters of the wild-type MSODs. All the M−N(His I) distances (∼2.4−2.6 Å), trans to the bound OH^-, (see Table 6 and Figure 1) are very long and are longer than those of their $M^{2+}(H_2O)$ counterparts by ∼0.2−0.4 Å. This contrasts the trend in M−O(V) and O(V)···N(Gln(X)) distances, which are much shorter than in the corresponding $M^{2+}(H_2O)$ clusters. Here, the fact is that the large negative charge on the OH^- group forces the metal center to go "up" toward the Gln(X) side chain to form a very strong H-bond between O(V) and $H_{\epsilon 22}$(X). The distance of O(V)···$H_{\epsilon 22}$(Gln151) in the optimized $Mn^{2+}(OH^-)$ of 3MDS is only 1.589 Å. As a result, the M^{2+}−His(I) bond and the $O_{\delta 1}$(Asp(IV))··· H(OH^-(V)) H-bond will be broken or nearly broken. From the structural character of the calculated $M^{2+}(OH^-)$ clusters

alone, $M^{2+}(OH^-)$ cannot be the resting form of M(II)SOD. Later, we will show that this result is also implied from the analysis of the proton equilibrium for the M^{2+} complexes.

In the first half cycle of Scheme 1 (eq 9), a superoxide anion O_2^- first binds and shares an electron with the M^{3+} center of $M^{3+}(OH^-)$SOD and then donates the electron to the metal center and leaves as an O_2 molecule. The rate constants describing the combination and the decomposition of $M^{3+}(OH^-)-O_2^-$ are k_1 and k_2, respectively. Bull et al.[21] obtained $k_1 = 2 \times 10^9$ M^{-1} s^{-1} and $k_2 = 1.2 \times 10^4$ s^{-1} for the catalysis by *T. thermophilus* MnSOD. k_1 is quite large and near the diffusion controlled limit. All kinetic studies for MSODs show that k_2 is relatively small. We propose that the superoxide anion O_2^- cannot donate the electron to the M^{3+} center and leave as an O_2 molecule immediately upon binding, because the presence of the negatively charged OH^- group on site V prevents this electron transfer. After binding with O_2^-, the metal center is not as positive as before, the M−O(V) distance hence becomes longer (see Tables 4 and 6), and the net negative charge on group OH^- pulls the metal center and the side chain of Gln(X) closer. Finally, we suppose a chain reaction occurs in which protons successively transfer along the appropriate H-bonding pathway. The proton $H_{\epsilon 22}$ on the side chain of Gln(X) will transfer to the OH^-(V) group, the H on the hydroxyl group of Tyr(XI) side chain will go to $N_{\epsilon 2}$ of Gln(X), and the O(Tyr(XI)) site will get a proton from its surrounding water molecules (there are always several water molecules around the hydroxyl group of Tyr(XI) in both chain A and chain B of each crystal structure). With a water molecule now bound as the fifth ligand, the O_2^- group will easily transfer the electron to the metal center and leave as an O_2 molecule, giving the $M^{2+}(H_2O)$ form of MSOD depicted in the first half of Scheme 1.

The assumption of proton transfers upon O_2^- binding to the $M^{3+}(OH^-)$ center is consistent with spectroscopic data on the azide adducts of Mn^{3+}SOD.[62,63] It was found that the Mn^{3+}SOD−azide complex is temperature dependent, exhibiting thermochromism and changing from a lower temperature six-coordinate form to a higher temperature five-coordinate form. It was supposed that a proton transferred to the hydroxyl group, forming a H_2O, or alternatively further transferred to reside on the aspartic acid.[63] The five-coordinate form may therefore result either from desolvation of the water molecule or from dissociating the protonated carboxylate group.

For investigating the function of residue Tyr(XI), Guan et al. have replaced Tyr34 with Phe34 (mutant Y34F) in hMnSOD and performed kinetic and spectroscopic studies.[23] The H-bonding chain mentioned previously becomes broken in the mutant Y34F. The kinetic results show that the replacement of Tyr34 → Phe does not affect the diffusion controlled steady-state constant k_{cat}/K_m, which has a value near 10^9 M^{-1} s^{-1} for both wild-type and Y34F hMnSOD.[23] However, the Tyr34 → Phe replacement does affect the rate of maximal catalysis k_{cat}, reducing by about 10-fold the steps that determine k_{cat}.[23] Comparing the kinetic rate constants in the forward direction (k_1, k_2, k_3, and k_4) for both wild-type (wt) and Y34F hMnSOD (see Scheme 1 and Table 3 of ref 23), we find that k_1(Y34F) = k_1(wt) = k_3(Y34F) = k_3(wt) = 2×10^9 M^{-1} s^{-1}, k_2(Y34F) = 5×10^3 s^{-1} < k_2(wt) = 8×10^4 s^{-1}, and k_4(Y34F) = 1×10^4 s^{-1} < k_4(wt) = 8×10^4 s^{-1}. These numbers show that the main differences of the catalysis by these two enzymes are within steps 2 and 4, where the catalysis by Y34F is much slower than that by wild-type hMnSOD, and especially, step 2 is the most difficult process for Y34F in the catalysis. This further proves our assumption that proton transfer will happen in step 2, and the proton transfer will occur prior to or concerted with the electron transfer from superoxide O_2^- group to the M^{3+}SOD metal center. This is a reason, in addition to the $M^{2+}(H_2O)$ pK_a energetics (see later in this work and analysis in refs 30,31), why we included the proton-transfer process in both reactions 9 and 10, rather than putting two protons in reaction 10 or the second half of Scheme 1. Though k_2(Y34F) is much slower than k_2(wt), Y34F remains active catalytically, suggesting the proton-transfer mechanism is still maintained in some form. We therefore examined the crystal structures of the Y34F proteins and found water molecules surrounding the side chain of Phe34 in each active site. In the orthorhombic crystal form Y34F (PDB code: 1AP5, 2.2 Å resolution), the water molecule HOH10 is 4.064 Å away from atom Gln143B $N_{\epsilon 2}$, and HOH620 is 5.155 Å away from Gln143A $N_{\epsilon 2}$. In another hexagonal crystal form of Y34F (PDB code: 1AP6, 1.9 Å resolution), the distance is 4.596 Å between HOH239 O and Gln143B $N_{\epsilon 2}$ and 6.739 Å between HOH26 O and Gln143A $N_{\epsilon 2}$. It certainly requires additional time for the system to reorganize the orientation of the Phe34 side chain and the water molecules nearby so that the water molecules can move closer to Gln143 and link with other residues in the H-bonding network. The chain reaction of proton transfers may still happen in the $Mn^{3+}(OH^-)$(Y34F)$-O_2^-$ active centers but more slowly than in the wild-type enzyme.

Very recently, Edwards et al.[64] reported that mutation of either His30 or Tyr174B in *E. coli* MnSOD reduces the activity to 30−40% of that of the wild-type enzyme. These two residues are highly conserved and correspond to His30 and Tyr166B in hMnSOD, His32 and Tyr173B in *T. thermophilus* MnSOD, and His30 and Tyr163B in *E. coli* FeSOD. Silverman and co-workers[65] found that mutation of any residue in the H-bonding network of Gln143···Tyr34···H_2O···His30···Tyr166B in hMnSOD will decrease the catalytic activity. This extended H-bonding network may therefore be the complete proton-transfer pathway.

The largest difference between the optimized $M^{3+}(OH^-)$ and $M^{2+}(H_2O)$ clusters is in the distance of the $M^{3+/2+}$ and O(V). The M^{2+}−O(V) bond lengths are about 0.5 Å longer than the corresponding M^{3+}−O(V) structures (see Tables 4 and 7). We have commented previously that redox heterogeneity is very likely in the "oxidized" MnSOD X−ray

(62) Whittaker, M. M.; Whittaker, J. W. *Biochemistry* **1996**, *35*, 6762.
(63) Whittaker, M. M.; Whittaker, J. W. *Biochemistry* **1997**, *36*, 8923.
(64) Edwards, R. A.; Whittaker, M. M.; Whittaker, J. W.; Baker, E. N.; Jameson, G. B. *Biochemistry* **2001**, *40*, 4622.
(65) Silverman, D. N. Private communication.

structures,[31] consistent also with EPR results.[28] This affects measured $M^{3+}-O(V)$ bond lengths. Other $M^{2+/3+}-$ligand distances in the optimized clusters are quite similar to those in the crystal structures. The water molecule on site V of a $M^{2+}(H_2O)$ cluster has a weaker interaction with M^{2+} but stronger H-bonding interaction with Asp(IV), by comparison with the corresponding OH^- group in $M^{3+}(OH^-)$. As a result, the O(IV)···O(V) distances in $M^{2+}(H_2O)$ structures are about 0.3 Å shorter than the corresponding ones in the $M^{3+}(OH^-)$ clusters (see Tables 4 and 7). Similar tendencies are observed in the reduced and oxidized *E. coli* FeSOD and *T. thermophilus* MnSOD crystal structures.

In the Gln143 → Asn (Q143N) hMnSOD mutant, during the $Mn^{2+}(OH^-)$ (see Figure 2, replacing the H_2O with OH^- on site V) geometry optimization calculations, the water molecule on site XIV transferred one proton (which originally H-bonded with OH^-(V)) to the OH^-(V) group. In the optimized geometry, the distances between this transferred proton and the two oxygen atoms O(V) and O(XIV) are 1.096 and 1.391 Å, respectively. The side chains of Asn143 and Tyr34 still have H-bonding interactions with the OH^-(XIV), and the H-bonding distances are r(Asn143 $H_{\delta 22}$···O(XIV)) = 1.851 Å and r(Tyr34 H···O(XIV)) = 1.466 Å. From the calculations, $Mn^{2+}(OH^-)$ is not a stable state for Q143N, and site V should be a water molecule for the resting state Mn(II)−Q143N metal center.

From the kinetic studies of Q143N by Hsieh et al.,[18] we have k_1(Q143N) = k_1(wt) = k_3(Q143N) = k_3(wt) = 2×10^9 M^{-1} s^{-1}, k_2(Q143N) = k_4(Q143N) = 6×10^2 s^{-1} < k_2(wt) = k_4(wt) = 8×10^4 s^{-1}, and k_{-1}(Q143N) = 1.5×10^6 s^{-1} > k_{-1}(wt) = 2×10^4 s^{-1}. These values show no difference for a superoxide anion to combine with Q143N or the wild-type hMnSOD, but the process for releasing the O_2 molecule from the complex $Mn-O_2^-$ is much slower in the Q143N mutant. The most likely reason is that the replacement of Gln143 by Asn alters the H-bonding pathway, making proton transfers more difficult. For the first half cycle of Scheme 1 (eq 9), when a superoxide anion O_2^- binds with the M^{3+} center of $M^{3+}(OH^-)$−Q143N, the OH^- on site V will lie slightly further from the metal ion and closer to the H_2O site XIV (because the metal center is less positive upon O_2^- binding). The proton of H_2O(XIV) which H-bonds with the OH^-(V) group will move closer to OH^-(V) and, as a result, may finally transfer to OH^-(V). A hydroxide is therefore left on site XIV, which still has three H-bonding partners, that is, H_2O(V), Tyr34(XI), and Asn143(X). This state may show a degree of short-term stability because the side chains of Tyr34(XI) and Asn143(X) compete with each other to interact with the OH^-(XIV). The transfer of a proton from Tyr34(XI) and Asn143(X) to OH^-(XIV) becomes difficult. This may be the reason that k_2 is only 6×10^2 s^{-1} in the catalysis by Q143N. Compared to Y34F (where k_{-1}(Y34F) = 1×10^3 s^{-1} < k_{-1}(wt) = 2×10^4 s^{-1}),[14] k_{-1} is much larger for the Q143N mutant (1.5×10^6 s^{-1}) than for wt hMnSOD (2×10^4 s^{-1}). Therefore, the tendency for $Mn-O_2^-$ to dissociate back to the reactants is considerably larger in the Q143N mutant. This is consistent with a necessity for proton binding (from $Mn-OH^-$ to $Mn-H_2O$) to facilitate electron transfer from O_2^- to the Mn. In the absence of proton transfer, the binding of O_2^- to the Mn^{3+}SOD metal center either forms a more stable $Mn-O_2^-$ complex (in Y34F) or rapidly dissociates back to the reactants (in Q143N). Finally, we suppose that proton transfers will occur along the pathway of OH^-(XIV)···Tyr34(XI)···H_2O···His30···Tyr166B in the Q143N mutant. (In the crystal structure of Q143N (PDB code: 1QNM), a water molecule (HOH111) is 2.706 Å away from the atom Tyr34A O, and HOH32 is 3.120 Å away fromTyr34B O.)

To examine if the oxidation state of chain B influences the redox potential of chain A, we calculated the protein and reaction field energies E_{pr}(III) and E_{pr}(II) (see Tables 4−7), pK_a values, and the coupled redox potentials of the active site clusters by treating the active site of chain B as $M^{3+}(OH^-)$ and $M^{2+}(H_2O)$ forms, respectively (see section 4). Calculated values of E_{pr}(III) and E_{pr}(II) for a particular cluster state are very similar to each other, and the oxidation state of chain B does not influence the pK_a's and the coupled redox potentials of the active site clusters of chain A. We will therefore only present our pK_a and redox potential results by treating the active site of chain B as $M^{2+}(H_2O)$.

5.2.2. Simple Redox Potentials and Absolute pK_a Values. The simple redox potentials for reactions $M^{3+}(OH^-) + e^- \rightarrow M^{2+}(OH^-)$ ($\Delta E_{redox}°[M(OH^-)]$) and $M^{3+}(H_2O) + e^- \rightarrow M^{2+}(H_2O)$ ($\Delta E_{redox}°[M(H_2O)]$) have been calculated according to eq 18. The results together with IP_{red} and ΔE_{pr}(redox) values are shown in Table 8. Similar to our previous calculations,[31] all $\Delta E_{redox}°[M(OH^-)]$ values are negative, and $\Delta E_{redox}°[M(H_2O)]$ values are positive. The negative sign for $\Delta E_{redox}°[M(OH^-)]$ indicates that $M^{2+}(OH^-)$ is less stable than the $M^{3+}(OH^-)$ form (relative to a standard hydrogen electrode), and the positive sign for $\Delta E_{redox}°[M(H_2O)]$ means that $M^{2+}(H_2O)$ is more stable than the $M^{3+}(H_2O)$ form of SOD. In the optimized $M^{2+}(OH^-)$ structure of Q143N (PDB: 1QNM), the fifth ligand is a water molecule rather than a OH^- group because it obtained a proton from the water molecule on site XIV. This $M^{2+}(OH^-)$ structure is therefore relatively more stable upon comparison with other $M^{2+}(OH^-)$ clusters, and its $\Delta E_{redox}°[M(OH^-)]$ (−0.28 V) is algebraically the highest among the negative $\Delta E_{redox}°[M(OH^-)]$ numbers.

The absolute pK_a values for $M^{2+}(H_2O)$ and $M^{3+}(H_2O)$ clusters were calculated according to eq 19. The pK_a results together with proton affinity PA and ΔE_{pr}(deproton) values are shown in Table 9. As far as we know, there are no experimental pK_a data for ligated water in MSODs. The positive pK_a values for the $M^{2+}(H_2O)$ forms indicate that $M^{2+}(H_2O)$ is very basic, and the $M^{2+}(H_2O)$ cluster is more

(66) Previously, the coupled redox potential for MnSOD from *T. thermophilus* was calculated on the basis of several smaller models.[31] The predicted absolute redox potential for Model D was +0.06 V, which is closer to the experimental value from reaction kinetics (0.40 V, see Table 2). In Model D,[31] however, simple NH_3 groups in the quantum cluster replaced the main chain amide groups of His170 and Trp168 (analogous to residues III and IX in the current work, see Table 1 and Figure 1), which causes difficulty in properly assigning the cluster and protein charges for the linking atoms of NH_3.

(67) Schaftenaar, G.; Noordik, J. H. *J. Comput.-Aided Mol. Des.* **2000**, *14*, 123.

(68) Sato, T.; Smith, B. V. *XFIG Drawing Program for X Window System*; 1997−2000.

Table 8. Calculated Simple Redox Potentials[a]

protein	FeSOD 1ISA	FeSOD 1ISB	MnSOD *T.T.* (red.)[b]	MnSOD 3MDS	MnSOD 1VEW	MnSOD 1ABM	MnSOD 1QNM
			$M^{3+}(OH^-) + e^- \rightarrow M^{2+}(OH^-)$				
IP_{red}[c]	2.5610	2.5213	2.2763	2.2384	2.5933	2.3462	2.9130
ΔE_{pr}(redox)[d]	1.2276	1.2388	1.2949	1.2783	1.2357	1.2345	1.2333
$\Delta E_{redox}°[M(OH^-)]$[e]	−0.64	−0.67	−0.86	−0.91	−0.60	−0.85	−0.28
			$M^{3+}(H_2O) + e^- \rightarrow M^{2+}(H_2O)$				
IP_{red}[f]	6.0930	6.1078	6.1803	6.1149	6.1199	6.0073	6.1235
ΔE_{pr}(redox)[g]	−0.1587	−0.1655	−0.4119	−0.7246	−0.3405	−0.3671	−0.2335
$\Delta E_{redox}°[M(H_2O)]$[e]	1.50	1.51	1.21	0.96	1.35	1.21	1.46

[a] Electronic and solvation energies (ΔE_{pr}(II)'s are used here) have been given in Tables 4−7. IP_{red} and ΔE_{pr}(redox) are in eV, and $\Delta E_{redox}°$ in V. [b] See footnote *b* of Table 1. [c] Obtained from $E[M^{3+}(OH^-)] - E[M^{2+}(OH^-)]$. [d] Calculated by $E_{pr}[M^{3+}(OH^-)] - E_{pr}[M^{2+}(OH^-)]$. [e] See eq 18. [f] Obtained from $E[M^{3+}(H_2O)] - E[M^{2+}(H_2O)]$. [g] Calculated by $E_{pr}[M^{3+}(H_2O)] - E_{pr}[M^{2+}(H_2O)]$.

Table 9. Calculated Absolute pK_a Results[a]

protein	FeSOD 1ISA	FeSOD 1ISB	MnSOD *T.T.* (red.)[b]	MnSOD 3MDS	MnSOD 1VEW	MnSOD 1ABM	MnSOD 1QNM
			$M^{2+}(OH^-) + H^+ \rightarrow M^{2+}(H_2O)$				
PA[c]	324.82	326.31	322.54	323.24	316.90	321.10	311.27
ΔE_{pr}(deproton)[d]	−29.02	−28.88	−30.64	−30.03	29.14	−30.37	−29.42
p$K_a[M^{2+}(H_2O)]$[e]	20.10	21.30	17.25	18.21	14.23	16.40	9.92
			$M^{3+}(OH^-) + H^+ \rightarrow M^{3+}(H_2O)$				
PA[c]	242.76	243.00	234.84	233.24	234.98	236.07	236.64
ΔE_{pr}(deproton)[f]	2.95	3.52	8.72	16.16	7.21	6.56	4.40
p$K_a[M^{3+}(H_2O)]$[e]	−16.46	−15.87	−18.03	−13.77	−19.03	−18.70	−19.87

[a] Electronic and solvation energies (ΔE_{pr}(II)'s are used here) have been given in Tables 4−7. PA and ΔE_{pr} in kcal/mol, and pK_a in pH units. [b] See footnote *b* of Table 1. [c] Proton affinity, see explanations of eq 19. [d] Calculated by $E_{pr}[M^{2+}(OH^-)] - E_{pr}[M^{2+}(H_2O)]$. [e] From eq 19. [f] Obtained from $E_{pr}[M^{3+}(OH^-)] - E_{pr}[M^{3+}(H_2O)]$.

Table 10. Comparison of the Coupled Redox Potentials $\Delta E_{Redox}°$(coupled, pH = 7) (V) Obtained from DF/Electrostatics and Reaction Kinetics Methods Together with Experimental Results

source	FeSOD *E. coli*		MnSOD *T. thermophilus*		MnSOD *E. coli*	MnSOD human mitochondria	
PDB code	1ISA	1ISB	*T.T.* (red.)[a]	3MDS	1VEW	1ABM (wild)	1QNM (Q143N)
DF/electrostatics[b]	0.14	0.18	−0.25	−0.25	−0.17	−0.29	−0.11
avg[c]	0.16		−0.25		−0.17	−0.29	−0.11
relative to *T.T.*[d]			0.00		0.08	−0.04	0.14
experiment							
reaction kinetics[e]			0.40			0.31	0.58
relative to *T.T.*[d]			0.00			−0.09	0.18
redox titration	0.25[f]				0.31[g]		

[a] See footnote *b* of Table 1. [b] Obtained from eq 20. [c] Average coupled redox potential for *E. coli* FeSOD and for *T. thermophilus* MnSOD from DF/electrostatics calculations. Values for other MnSODs do not change. [d] Relative values (relative to the $\Delta E_{redox}°$(coupled) of MnSOD from *T. thermophilus*) of the coupled redox potentials of MnSODs obtained from DF/electrostatics and reaction kinetics calculations. [e] Obtained from eqs 16 and 17. Also given in the last row of Table 2. [f] Taken from ref 26. Direct redox measurement result is 0.223 V at pH = 7.4. This value was extrapolated to 0.25 V at pH = 7 using eq 17. [g] Taken from ref 27. Direct redox measurement at pH = 7

stable than $M^{2+}(OH^-)$. Note that the calculated pK_a values for the wild-type $M^{2+}(H_2O)$SOD clusters are very positive (all larger than 14.0), which shows that for the resting state of M(II)SOD, only the $M^{2+}(H_2O)$ form and not the $M^{2+}(OH^-)$ form is likely to be significantly present.[31] This is consistent with our structural and energetic analysis in section 5.2.1.

The calculated pK_a for the mutant Q143N−$M^{2+}(H_2O)$ (9.92) is actually the pK_a for the water molecule on site XIV, which transfers a proton to the OH^- on site V. During the kinetic studies of catalysis by Q143N, Hsieh et al.[18] found an apparent pK_a near or below 8.5 for k_{cat}/K_m. This apparent pK_a may be related to this Q143N−$M^{2+}(OH^-)$ state with the transferred proton.

Conversely, the large negative pK_a values for $M^{3+}(H_2O)$ clusters indicate that, under normal pH conditions, only the $M^{3+}(OH^-)$ form exists for the M(III)SOD state. This is also consistent with our conclusions in section 5.2.1.

5.2.3. Coupled Redox Potentials. According to the calculated simple redox potential and pK_a values, we obtain the coupled redox potentials (at pH = 7) for each protein model using eq 20. In Table 10, we compare the coupled redox potentials calculated by the DF/electrostatics method (from eq 20) and by the reaction kinetics method (eqs 17), together with the available experimental results.

Our DF/electrostatics calculated $\Delta E_{redox}°$(coupled, pH = 7) for *E. coli* FeSOD is 0.16 V, which is the average of the two coupled redox potentials obtained from the two protein models, 1ISA and 1ISB. The experimental value is 0.25 V at pH = 7, which is extrapolated from the value 0.223 V at pH = 7.4 obtained from direct redox measurement by spectroelectrochemistry.

The coupled redox potentials of MnSODs calculated by the DF/electrostatics method are all negative and much lower than the results obtained from experimental kinetic rate constants. Taking the coupled redox potential of *T. thermophilus* MnSOD as a reference point, we obtained the relative coupled redox potential values of 0.00, −0.04, and 0.14 V from DF/electrostatics calculations for three MnSODs from *T. thermophilus*, human wild-type, and Q143N, respectively, and of 0.00, −0.09, and 0.18 V from the reaction kinetics method for these three MnSODs, respectively. The two methods, therefore, predict the same relative ordering and very similar relative values for the coupled redox potentials of the three MnSODs, that is, $\Delta E_{redox}°$(human wild) < $\Delta E_{redox}°$(*T. thermophilus*) < $\Delta E_{redox}°$(Q143N). This matching of $\Delta E_{redox}°$(coupled) from kinetics and quantum/reaction-field calculations further demonstrates that our DF/electrostatics model is reliable for predicting trends among related MnSOD enzymes.

There is only one experimental coupled redox potential, for MnSOD (from *E. coli*), obtained from direct electrochemical measurements to compare with the data here.[27] Our DF/electrostatics method predicted the absolute $\Delta E_{redox}°$(coupled, pH = 7) = −0.17 V for *E. coli* MnSOD, which is higher than those for human wild-type and *T. thermophilus* MnSODs. The experimental datum is 0.31 V obtained at pH = 7,[27] which is, however, the same as that of human wild-type MnSOD and lower than that of *T. thermophilus* MnSOD obtained from our reaction kinetics predictions. Note that for the same experiment at pH = 8, the measured redox potential changed to 0.32 V, which is even larger than the measured $\Delta E_{redox}°$(pH = 7) = 0.31 V. This conflicts with other observations of direct redox potential measurements, where the redox potentials decrease with the increasing pH.[27] We therefore suggest that the $\Delta E_{redox}°$(coupled, pH = 7) of *E. coli* MnSOD will be larger than 0.32 V, but additional experiments involving either direct redox measurements or reaction kinetics studies are required to reexamine this potential.

Our DF/electrostatics calculations here predict the order $\Delta E_{redox}°$(human wild-type) < $\Delta E_{redox}°$(*T. thermophilus*) < $\Delta E_{redox}°$(*E. coli*) < $\Delta E_{redox}°$(Q143N) for MnSOD proteins.

It seems that our DF/electrostatics method has larger intrinsic error for MnSOD systems than for FeSODs in predicting their coupled redox potentials. Our previous work also shows that the current method predicts a more accurate absolute coupled redox potential at pH = 7 for the $Fe^{3+/2+}$ aquo system ($Fe^{3+/2+}$ cations in solution) (calculated 0.41 V versus measured 0.48 V) and a larger deviation for $Mn^{3+/2+}$ aquo system (calculated 0.79 V versus measured 1.15 V).[34] This may be because the $Mn^{3+}(OH^-)$ clusters are overstabilized in the DF calculations, resulting in very negative pK_a-[$Mn^{3+}(H_2O)$] and $\Delta E_{redox}°$[$Mn(OH^-)$] values and showing proton transfer from the ligand water molecule to aspartic acid during geometry optimization processes for all Mn^{3+}-(H_2O) clusters. This proton transfer may still be correct, but this is not yet resolved.

6. Conclusions

In this paper, we have presented for the first time the methodology to deduce the coupled redox potential from the standard redox potential of reaction ($O_2^- + 2H^+ + e^- \rightarrow H_2O_2$) and the experimental kinetic rate constants for Mn(Fe)SOD proteins. The coupled redox potentials for *T. thermophilus*, human wild-type, and mutant Q143N MnSODs have been obtained from the experimental kinetic rate constants; they are 0.40, 0.31, and 0.58 V, respectively. This scheme provides a valuable alternative to spectroelectrochemistry (with mediators).

Using the combined density functional (DF) and electrostatic protein/reaction field (DF/electrostatics) method, we have studied the structural, energetic, simple redox potential, pK_a, and, finally, coupled redox potential properties for seven Mn(Fe)SOD structures from five independent proteins, that is, *E. coli* FeSOD and *T. thermophilus*, *E. coli*, human wild-type, and mutant Q143N MnSODs. All geometry optimization and pK_a and simple redox potential calculations show that the resting state of a Mn(Fe)(III)SOD is in Mn^{3+}-(Fe^{3+})(OH^-) form, and the Mn(Fe)(II)SOD in $Mn^{2+}(Fe^{2+})$-(H_2O) form. From the structural and energetic characteristics of the $Mn^{2+}(Fe^{2+})(OH^-)$ and $Mn^{2+}(Fe^{2+})(H_2O)$ clusters, and the experimental kinetic rate constant values, we conclude that proton transfer happens in both steps of the catalytic cycle, that is,

$$Mn^{3+}(Fe^{3+})(OH^-) + O_2^- + H^+ \rightarrow Mn^{2+}(Fe^{2+})(H_2O) + O_2 \quad \text{(I)}$$

and

$$Mn^{2+}(Fe^{2+})(H_2O) + O_2^- + H^+ \rightarrow Mn^{3+}(Fe^{3+})(OH^-) + H_2O_2 \quad \text{(II)}$$

rather than considering the $2H^+$ only in the second step (II). In the first step (I), the chain reaction of the proton transfers will occur prior to or concerted with the electron transfer from superoxide O_2^- group to the $Mn^{3+}(Fe^{3+})$SOD metal center. To clearly understand how protons transfer in the active site, an investigation of the Mn(Fe)SOD catalytic mechanisms that includes the binding of the O_2^- group to the $Mn^{3+/2+}(Fe^{3+/2+})$ centers is required. This aspect of the catalysis we propose to study in the future.

The $\Delta E_{redox}°$(coupled) of *E. coli* FeSOD calculated by the DF/electrostatics method is 0.16 V, which is very close to the experimental result of 0.25 V (at pH = 7). The absolute values of coupled redox potentials of *T. thermophilus*, human wild-type, and mutant Q143N MnSODs obtained from the DF/electrostatics method are −0.25, −0.29, and −0.11 V, which show the same trend as those obtained from experimental kinetic rate constants (0.40, 0.31, and 0.58 V, respectively). Our calculations predict coupled redox potentials with the following ordering: $\Delta E_{redox}°$(human wild-type) < $\Delta E_{redox}°$(*T. thermophilus*) < $\Delta E_{redox}°$(*E. coli*) < $\Delta E_{redox}°$(Q143N) for MnSOD proteins.

Acknowledgment. This work was supported by NIH Grant GM50154. We thank M. L. Ludwig, J. A. Tainer, Y.

Guan, J. A. Fee, D. N. Silverman, E. Stroupe, and C. Fisher for valuable insights into SOD structures and properties. We are grateful to M. L. Ludwig and A. L. Metzger for giving us the crystallographic data of reduced *T. thermophilus* MnSOD. Special thanks to D. N. Silverman for valuable discussions about the kinetic rate constants. We thank D. Bashford for providing us the MEAD code. We thank J. Li, G. M. Ullmann, and T. Liu for discussions and assistance with the implementation of many programs. The generous support of CPU time on the SGI clusters of the Scripps Research Institute is also gratefully acknowledged.

IC010355Z